Acta Pharmaceutica Sinica B 2022;12(4):2074–2088

Chinese Pharmaceutical Association
Institute of Materia Medica, Chinese Academy of Medical Sciences

Acta Pharmaceutica Sinica B

www.elsevier.com/locate/apsb
www.sciencedirect.com

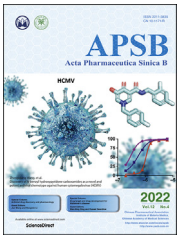

ORIGINAL ARTICLE

"Pincer movement": Reversing cisplatin resistance based on simultaneous glutathione depletion and glutathione *S*-transferases inhibition by redox-responsive degradable organosilica hybrid nanoparticles

Boyi Niu[a,†], Yixian Zhou[a,†], Kaixin Liao[a], Ting Wen[a], Sixian Lao[a], Guilan Quan[b,*], Xin Pan[a,*], Chuanbin Wu[a,b,*]

[a]*School of Pharmaceutical Sciences, Sun Yat-sen University, Guangzhou 510006, China*
[b]*College of Pharmacy, Jinan University, Guangzhou 510632, China*

Received 20 July 2021; received in revised form 30 September 2021; accepted 4 October 2021

KEY WORDS

Cancer therapy;
Cisplatin;
Drug resistance;
Glutathione depletion;
Glutathione *S*-transferases;
Disulfide bonds;
Organosilica hybrid nanoparticles;
Ethacrynic acid

Abstract The therapeutic efficacy of cisplatin has been restricted by drug resistance of cancers. Intracellular glutathione (GSH) detoxification of cisplatin under the catalysis of glutathione *S*-transferases (GST) plays important roles in the development of cisplatin resistance. Herein, a strategy of "pincer movement" based on simultaneous GSH depletion and GST inhibition is proposed to enhance cisplatin-based chemotherapy. Specifically, a redox-responsive nanomedicine based on disulfide-bridged degradable organosilica hybrid nanoparticles is developed and loaded with cisplatin and ethacrynic acid (EA), a GST inhibitor. Responding to high level of intracellular GSH, the hybrid nanoparticles can be gradually degraded due to the break of disulfide bonds, which further promotes drug release. Meanwhile, the disulfide-mediated GSH depletion and EA-induced GST inhibition cooperatively prevent cellular detoxification of cisplatin and reverse drug resistance. Moreover, the nanomedicine is integrated into microneedles for intralesional drug delivery against cisplatin-resistant melanoma. The *in vivo* results show that the nanomedicine-loaded microneedles can achieve significant GSH depletion, GST inhibition, and consequent tumor growth suppression. Overall, this research provides a promising strategy for the construction of new-type nanomedicines to overcome cisplatin resistance, which extends the biomedical application of organosilica hybrid nanomaterials and enables more efficient chemotherapy against drug-resistant cancers.

*Corresponding authors. Tel./fax: +86 20 39943115 (Guilan Quan); +86 20 39943427 (Xin Pan); +86 20 39943117 (Chuanbin Wu).
E-mail addresses: quanguilan@jnu.edu.cn (Guilan Quan), panxin2@mail.sysu.edu.cn (Xin Pan), wuchuanb@mail.sysu.edu.cn (Chuanbin Wu).
†These authors made equal contributions to this work.
Peer review under responsibility of Chinese Pharmaceutical Association and Institute of Materia Medica, Chinese Academy of Medical Sciences

https://doi.org/10.1016/j.apsb.2021.10.013

1. Introduction

Cisplatin (CisPt) has been one of the most widely used first-line chemotherapeutic drugs in the therapeutic regimens of various types of cancer, including ovarian cancer[1], head and neck squamous cell carcinoma[2], non-small cell lung cancer[3], and melanoma[4]. The predominant antitumor mechanism of CisPt is considered to be the generation of DNA lesions induced by the binding of platinum (Pt) to DNA, which triggers DNA damage response and further cell apoptosis[5]. However, the clinical application of CisPt-based chemotherapy is greatly restricted by drug resistance and side effects in the long-term systemic administration[3]. Multiple mechanisms have been proposed to participate in the development of CisPt resistance, including reduced intracellular drug accumulation, detoxification of drug by endogenous nucleophiles like glutathione (GSH) and metallothioneins, increased DNA repairing activity, and changes of signal pathways related to apoptotic regulation[6−10]. Among these, GSH and glutathione *S*-transferases (GST) play important roles in the defense against electrophilic xenobiotics in cancer cells. In some reports, the elevated levels of GSH and GST were observed in CisPt-resistant cancer cells, which suggested their correlations with drug resistance[11−13]. After endocytosis by cells, CisPt can be directly conjugated with GSH under the catalysis of GST, forming a GS-Pt conjugate that is further extruded by cells[14−16]. This detoxification process reduces the intracellular content of active Pt, resulting in the weakening of drug efficacy and the development of drug resistance. Therefore, depleting GSH or inhibiting GST can be effective ways to prevent cellular detoxification of CisPt and reverse CisPt resistance.

A variety of molecules including L-buthionine sulfoximine (BSO)[17], sanguinarine[18], and sulforaphane[19] have been reported to consume GSH and restore cellular sensitivity to Pt-based drugs. Several GST inhibitors, such as ethacrynic acid (EA)[15], TLK199[20], and auranofin[21] were also shown to be able to sensitize cancer cells to anticancer drugs. Although these studies have proved the efficacy of GSH depletion or GST inhibition on the chemosensitization of drug-resistant cancers, cancer cells might restore their intracellular GSH levels by upregulating the expression of relevant synthetases[22,23]. In such situations, unilateral intervention is usually not enough to destroy the cellular detoxification process. Combination therapy with multiple active substances is expected to achieve better therapeutic efficacy. Nevertheless, separate delivery of these molecules and CisPt probably cannot achieve the best efficacy due to inconsonant time to peak within cancer cells. In addition, free CisPt is internalized by cells mainly *via* copper transporter 1 (CTR1)[24,25], the expression of which was reported to be down-regulated in some CisPt-resistant cells[26]. This change might reduce the cellular Pt uptake and also weaken the efficacy of chemotherapy. Nanotechnology may be able to solve these problems as nanoparticles can deliver multiple drugs and bypass the CTR1 pathway through endocytosis[27,28]. Besides, in recent years, functional nanoparticles were designed to achieve intracellular GSH depletion by themselves, such as disulfide bonds (S−S)-containing nanoparticles[29], phenylboronic ester moieties-containing micelles[30], gold nanoclusters[16], and iodide-containing nanoparticles[31]. These functional nanoparticles made full use of the carriers themselves and reduced the difficulty of the loading and delivery of multiple drugs.

Mesoporous silica nanoparticles (MSNs) are a kind of nanomaterials with many unique features. The porous structure, large specific surface area, and good biocompatibility of MSNs make them ideal drug delivery carriers for versatile guest molecules[32]. In addition, MSNs can be flexibly functionalized as required by group modification on the surface and organic-inorganic hybridization within the framework[33]. Herein, we designed a redox-responsive nanomedicine, (CisPt+EA)@SHMONs, to execute "pincer movement" for reversing CisPt resistance (Fig. 1). The nanomedicine was constructed based on S−S-bridged hollow mesoporous organosilica hybrid nanoparticles (SHMONs), which were co-loaded with CisPt and EA, a GST inhibitor. After endocytosis by cancer cells, SHMONs would be gradually degraded responding to the intracellular GSH and accompanied by the release of two encapsulated drugs. This process would deplete a large number of GSH and consequently reduce the possibility of its conjugation with CisPt, which acted as one piece of the "pincer". Meanwhile, the released EA could inhibit the activity of GST and prevent GST-catalyzed conjugation between GSH and CisPt, which acted as another piece of the "pincer". As a result of this "pincer movement", (CisPt+EA)@SHMONs could effectively prevent cellular GSH detoxification of CisPt and exhibited strong cell-killing ability against CisPt-resistant A375/DDP cells. In addition, we integrated this nanomedicine into microneedles (MN) for the treatment of CisPt-resistant melanoma by directly depositing the nanomedicine into the lesion site without systemic circulation. The *in vivo* results showed that significant inhibiting effects on tumor growth were achieved by the nanomedicine, indicating successful reversal of CisPt resistance. Therefore, this research provides a valuable strategy for reversing CisPt resistance by simultaneous depleting GSH and inhibiting GST, which is expected to enhance the therapeutic efficacy of chemotherapy.

2. Materials and methods

2.1. Materials, cell lines, and animals

Tetraethyl orthosilicate (TEOS), cetyltrimethylammonium chloride (CTAC), triethanolamine (TEA), fluorescein isothiocyanate (FITC), Cy5.5-NHS ester, 1,4-dithiothreitol (DTT), 5,5′-dithio bis-(2-nitrobenzoic acid) (DTNB), and EA were obtained from Aladdin Industrial Inc. (Shanghai, China). Bis(triethoxysilylpropyl) disulfide (BTDS) and 1,2-bis(triethoxysilyl)ethane (BTEE) were obtained from Gelest Inc. (Morrisville, USA). (3-Aminopropyl) triethoxysilane (APTES) and GSH were purchased from Sigma−Aldrich (St. Louis, USA). CisPt was purchased from Shandong Boyuan Pharmaceutical Co., Ltd. (Jinan, China). Tris(2-carboxyethyl)phosphine hydrochloride (TCEP·HCl) was obtained from Shanghai Macklin Biochemical Co., Ltd. (Shanghai, China).

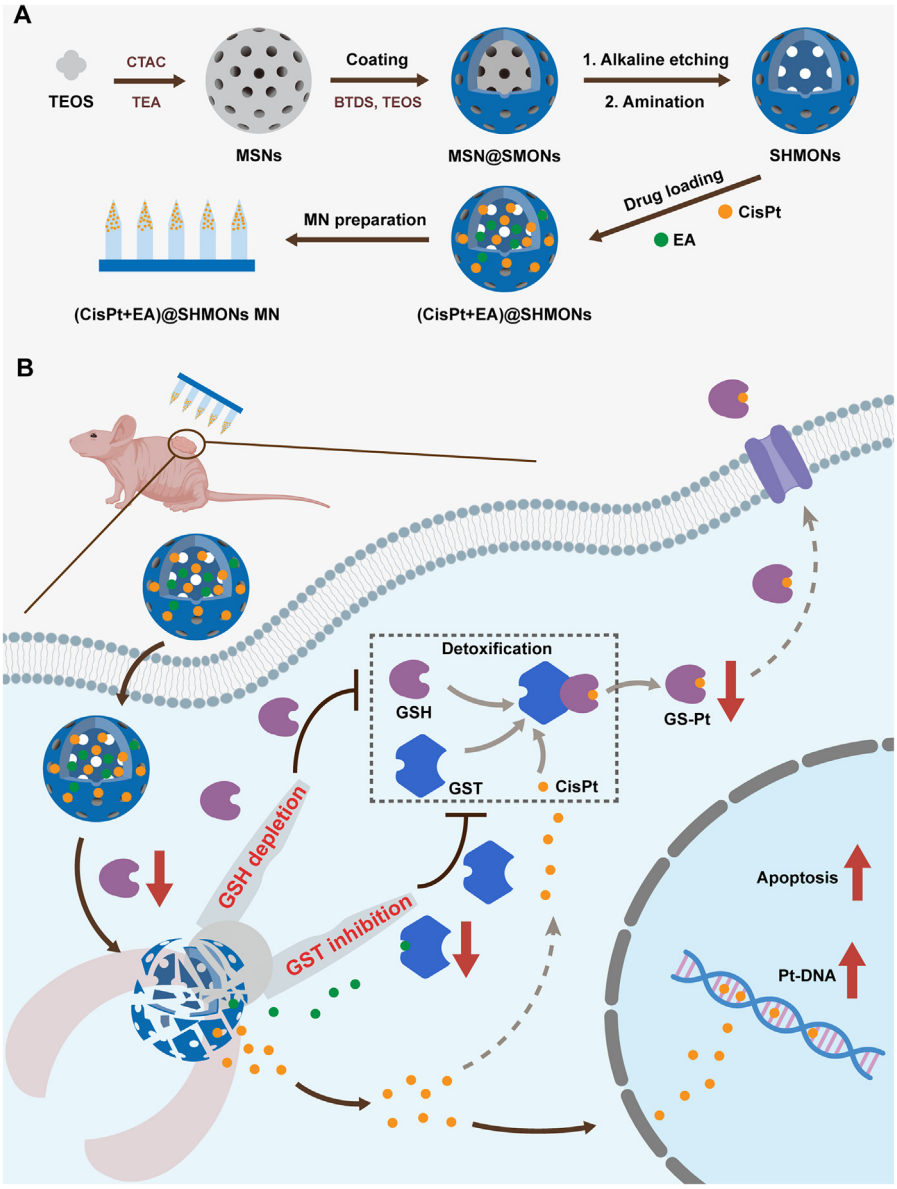

Figure 1 Schematic illustration of the nanomedicine (CisPt+EA)@SHMONs to execute "pincer movement" for reversing CisPt resistance. (A) Synthesis of SHMONs and preparation of (CisPt+EA)@SHMONs MN. (B) Application of (CisPt+EA)@SHMONs MN at the lesion of CisPt-resistant melanoma, the following cellular internalization, and mechanism of action. High level of intracellular GSH promoted the degradation of SHMONs and the subsequent release of CisPt and EA. This SHMONs-mediated GSH depletion was expected to reduce the conjugation of GSH to CisPt, which acted as one piece of the "pincer". In addition, the released EA-mediated GST inhibition could further prevent GST-catalyzed conjugation between GSH and CisPt, which acted as another piece of the "pincer". This nanomedicine based on simultaneous GSH depletion and GST inhibition would prevent GSH detoxification of CisPt, increase the generation of Pt-DNA adducts, and eventually enhance cancer cell apoptosis.

BSO was purchased from MedChemExpress (Monmouth Junction, USA). LysoTracker Red DND-99 was purchased from Yeasen Biotech Co., Ltd. (Shanghai, China). Hoechst 33342 was purchased from Beyotime Biotechnology (Shanghai, China). 2,7-Dichlorodihydrofluorescein diacetate (DCFH-DA) was purchased from Solarbio (Beijing, China). Sodium hyaluronic acid (HA) was obtained from Bloomage Biotechnology Co., Ltd. (Jinan, China). Polyvinylpyrrolidone K90 (PVP K90, Kollidon® 90 F) was obtained from BASF (Ludwigshafen, Germany). Matrigel was purchased from Corning Inc. (Bedford, USA).

CisPt-resistant human malignant melanoma cell line A375/DDP cells and CisPt-sensitive human malignant melanoma cell line A375 cells were cultured in DMEM medium (Gibco, Suzhou, China) supplemented with 10% fetal bovine serum (Gibco, South America) at 37 °C in a humidified atmosphere containing 5% CO_2.

BALB/c nude mice (female, 4−6 weeks old) were purchased from Guangdong Medical Laboratory Animal Center. All the animal experiments were approved by the Institutional Animal Care and Use Committee, Sun Yat-sen University.

2.2. Synthesis of SHMONs

SHMONs were synthesized according to the literature with minor modification[34]. Briefly, 4.0 g of CTAC and 0.16 g of TEA were separately dissolved in water to prepare 10% (*w*/*w*) solution. The two solutions were mixed at 95 °C for 20 min, followed by the dropwise addition of 2 mL of TEOS. MSNs were obtained after 1 h of reaction. A mixture of TEOS and BTDS was added dropwise to the above solution. After reaction for 4 h, MSN@SMONs with S−S-containing organosilica coating were collected by centrifugation and washed with absolute ethanol for three times. The surfactant CTAC was removed by three repeated extraction processes in the mixed solution of hydrochloric acid (HCl) and ethanol (V_{HCl}:$V_{ethanol}$ = 10:1) at 78 °C for 12 h. The MSN@SMONs were dispersed in 400 mL of water, followed by adding 8 mL of ammonia solution and reacting at 95 °C for 3 h to etch the inner core. The nanoparticles were collected, washed with water for three times, and dispersed in ethanol. For amination, 2 mL of APTES was added into the above suspension and reacted at 78 °C for 12 h. SHMONs were collected, washed, and dispersed in ethanol for further use.

To prepare control nanoparticles HMONs without S−S, BTDS was replaced with BTEE during synthetic process. To prepare FITC-labeled SHMONs (FITC-SHMONs), 9 mg of FITC and 60 μL of APTES were dispersed in 5 mL of absolute ethanol and reacted in the dark at ambient temperature for 4 h. Then, 60 mg of SHMONs in 25 mL of absolute ethanol were added into the above solution. After reaction for 24 h, the FITC-SHMONs were collected, washed, and dried in vacuum. To prepare Cy5.5 labeled-SHMONs (Cy5.5-SHMONs), 100 mg of SHMONs were dispersed in 10 mL of phosphate buffer saline (PBS) buffer (pH 8.0). Then, 1 mg of Cy5.5-NHS was dissolved in 1 mL of DMSO and added into the above suspension. After reaction in the dark for 24 h, the Cy5.5-SHMONs were collected, washed, and dried in vacuum.

2.3. Characterization of SHMONs

The morphology of the samples was characterized by field emission scanning electron microscopy (SEM; Gemini500, Zeiss, Germany). The structure of SHMONs was observed by transmission electron microscopy (TEM; FEI Talos F200X, FEI, USA) at an accelerating voltage of 200 kV. The elemental distribution of SHMONs was analyzed by high-angle annular dark-field scanning TEM (HAADF-STEM) equipped with energy dispersive X-ray spectrometry (EDX) for elemental analysis. Zeta potentials of the samples were measured by a laser particle size and zeta potential analyzer (Zetasizer Nano ZS90, Malvern, UK). The nitrogen absorption−desorption analysis was conducted on a surface area and porosimetry analyzer (ASAP 2460, Micromeritics, USA). The thermogravimetric analysis was conducted using a thermal gravimetric analyzer (TGA; TG209F1 Libra, Netzsch, Germany). The chemical structure of SHMONs was characterized by solid-state cross polarization/magic angle spinning ^{13}C and ^{29}Si nuclear magnetic resonance spectroscopy (NMR; Bruker Avance 400, Germany) and Fourier transform infrared spectroscopy (FT-IR; Nicolet 6700, Thermo Fisher Scientific, USA).

2.4. Redox-responsive degradation

Different samples (1.5 mg/mL in PBS) were mixed with DTT (5 mmol/L in PBS) and incubated at 37 °C for different duration (6, 24, and 96 h). At predetermined time points, the samples were centrifuged (GL-20B, Flying Pigeon, China) at 12,000 rpm for 10 min to collect the precipitates. The precipitates were washed and incubated with DTNB (5 mmol/L in PBS-EDTA) at ambient temperature for 10 min. Then the supernatants were collected by centrifugation and diluted to measure the absorbance at 412 nm using a UV−Vis spectrophotometer (TU-1901, Beijing Purkinje General Instrument Co., Ltd.). To characterize the redox-responsive degradation of SHMONs, the nanoparticles (0.1 mg/mL) were dispersed in PBS with or without 10 mmol/L of GSH and incubated at 37 °C for 7 days. On Days 1, 4, and 7, 1 mL of nanoparticle suspensions were collected by centrifugation for morphological observation by TEM (FEI).

2.5. In vitro cellular uptake of SHMONs

FITC-SHMONs were used to characterize the cellular uptake of SHMONs. For confocal laser scanning microscope (CLSM) observation, A375/DDP cells were seeded in glass-bottom culture dishes (15 mm) at a density of 2.5×10^5 cells and cultured overnight. Then, the old culture medium was replaced with the fresh culture medium containing 40 μg/mL of FITC-SHMONs. After incubation for different duration (10 min, 30 min, 1 h, and 4 h), the cells were rinsed with PBS for three times to remove the extracellular nanoparticles. Next, the acidic organelles were stained with LysoTracker Red DND-99 (50 nmol/L) and incubated for 1 h. Then, Hoechst 33342 (4 μg/mL) was added to stain cell nucleus for 10 min. Finally, the cells were washed three times with PBS and observed by CLSM (FV3000, Olympus, Japan). For flow cytometry analysis, A375/DDP cells were seeded in six-well plates at a density of 5×10^5 cells per well. The incubation and drug treatment were same as above. Cells were digested with trypsin and analyzed using a flow cytometer (Guava easyCyte, Millipore, USA).

2.6. Intracellular GSH depletion

A375/DDP cells or A375 cells were seeded in six-well plates at a density of 4×10^5 cells per well and cultured overnight. The cells were treated with BSO (200 μmol/L), SHMONs (120 μg/mL), and HMONs (120 μg/mL) for 6 h, respectively. Then, the cells were rinsed with PBS and digested with trypsin. The collected cells were divided into two parts. One part was used to detect the GSH content using a GSH and GSSG Assay Kit (Beyotime Biotechnology, China), and the other part was used to detect the protein content using a BCA Protein Assay Kit (Beyotime Biotechnology, China).

2.7. Intracellular ROS detection

A375/DDP cells were seeded in glass-bottom culture dishes (15 mm) at a density of 2.5×10^5 cells per well and cultured overnight. The cells were treated with BSO (200 μmol/L), SHMONs (60 μg/mL), and HMONs (60 μg/mL) for 6 h. The cells were rinsed with PBS and incubated with DCFH-DA for 20 min. After that, the cells were washed to remove extracellular probe and observed by CLSM (Olympus).

2.8. Drug loading and release

To load CisPt and EA, 16 mg of SHMONs were initially dispersed in 8 mL of CisPt solution (0.5 mg/mL in saline) and stirred in the

dark for 24 h. Then, the CisPt-loaded nanoparticles (CisPt@SHMONs) were collected by centrifugation and washed to remove free drugs. Next, CisPt@SHMONs were dispersed in 8 mL of EA solution (2 mg/mL in ethanol) and stirred in the dark for another 24 h. Finally, the (CisPt+EA)@SHMONs were obtained after centrifugation and washing. For each drug loading step, the supernatant and washing solution were collected and determined to calculate the drug loading content. The Pt content was quantified by inductively coupled plasma-atomic emission spectrometry (ICP-AES; Optima 8300, PerkinElmer, USA). The EA content was quantified by UV−Vis spectrophotometer. Drug release was detected by dialysis method with TCEP·HCl as the reducing agent. Ten mg of drug-loaded nanoparticles were transferred into a dialysis bag (MWCO 8−14 kDa). The bags were immersed in 30 mL of PBS (pH 7.4) with or without 10 mmol/L of TCEP·HCl, which were incubated in a shaker at 37 °C. At predetermined time points, 20 mL of the release medium was sampled and replaced with equal amount of fresh medium. The Pt content was quantified by ICP-AES (PerkinElmer).

2.9. *In vitro cytotoxicity*

A375/DDP cells or A375 cells were seeded in 96-well plates at a density of 8000 cells per well and cultured overnight. The cells were treated with different concentrations of CisPt, EA, CisPt+EA, CisPt@SHMONs, (CisPt+EA)@SHMONs, and SHMONs. After incubation for 48 h, the culture medium was replaced with 100 μL of 3-(4,5-dimethylthiazol-2-yl)-2,5-diphenyltetrazolium bromide (MTT) solution (0.5 mg/mL). After incubation for another 4 h, 100 μL of formazan solvent was added and incubated until the formazan crystals were dissolved. The absorbance at 570 nm was measured with a microplate reader (BioTek Instruments, USA).

2.10. *In vitro cell apoptosis*

A375/DDP cells were seeded in six-well plates at a density of 2×10^5 cells per well and cultured overnight. The cells were treated with CisPt, EA, CisPt+EA, CisPt@SHMONs, and (CisPt+EA)@SHMONs (equal CisPt concentration of 6.4 μg/mL, equal EA concentration of 3.5 μg/mL) for 48 h. Then the cells were harvested, rinsed with PBS, and resuspended in 1× binding buffer. The cells were stained using an Annexin V-FITC/PI apoptosis kit (MultiSciences Biotech, China) and analyzed by flow cytometry.

2.11. *In vitro Pt uptake*

A375/DDP cells were seeded in six-well plates at a density of 3×10^5 cells per well and cultured overnight. The cells were treated with CisPt, CisPt+EA, and (CisPt+EA)@SHMONs (equal CisPt concentration of 6.4 μg/mL, equal EA concentration of 3.5 μg/mL) for 4 h. Then, the cells were rinsed with PBS and lysed with RIPA lysis buffer. The Pt content in cells was qualified by inductively coupled plasma mass spectrometry (ICP-MS; Thermo Fisher Scientific, USA) and the protein content was qualified using a BCA Protein Assay Kit.

2.12. *In vitro Pt-DNA adduct formation*

A375/DDP cells were seeded in 25 cm^2 cell culture flasks at a density of 1.5×10^6 cells and cultured overnight. The cells were treated with CisPt, CisPt+BSO (200 μmol/L), CisPt+EA, CisPt@SHMONs, and (CisPt+EA)@SHMONs (equal CisPt concentration of 6.4 μg/mL, equal EA concentration of 3.5 μg/mL) for 4 h. Then, the cells were rinsed with PBS and digested with trypsin. The genomic DNA in cells was extracted using a Genomic DNA Mini Preparation Kit with Spin Column (Beyotime Biotechnology, China). The DNA concentration was determined using a NanoDrop 2000 spectrophotometer (Thermo Fisher Scientific, USA). The Pt content in the extracted DNA was qualified by ICP-MS (Thermo Fisher Scientific).

2.13. *In vitro GST activity*

A375/DDP cells or A375 cells were seeded in 25 cm^2 cell culture flasks at a density of 2×10^6 cells and cultured overnight. The cells were treated with CisPt, CisPt+EA, and (CisPt+EA)@SHMONs (equal CisPt concentration of 6.4 μg/mL, equal EA concentration of 3.5 μg/mL) for 4 h. Then, the cells were rinsed with PBS and digested with trypsin. The cells were lysed by ultrasonication in the ice bath. The lysed solution was centrifuged at 8000×*g* for 10 min and supernatant crude enzyme was obtained. The GST activity was detected using a GST Assay Kit (Solarbio, China) and the protein content was measured using a BCA Protein Assay Kit.

2.14. *Preparation and characterization of MN*

For the preparation of the nanoparticles-loaded MN, 20 mg of the synthesized nanoparticles were ultrasonically dispersed in 1 mL of water, followed by addition of 200 mg of HA. After stirring for 1 h, the suspension was added to the surface of the polydimethylsiloxane (PDMS) female mold and centrifuged (DL-4000B, Flying Pigeon, China) at 4000 rpm for 5 min. The excess suspension on the mold surface was removed. Then, the mold was dried in the desiccator for 24 h. The above procedure was repeated three times before adding the PVP K90 ethanol solution (31.25%, *w*/*v*) to prepare the backing layer. The MN was demolded after drying for 48 h.

The morphology of MN was observed by portable microscope, stereomicroscope, and SEM. The distribution of the nanoparticles in MN was observed by CLSM using FITC-SHMONs-loaded MN. The excised skin obtained from SD rat and pig was used to evaluate the skin puncture ability of MN. The MN patch was pressed onto skin for 2 min and then remained for another 5 min. After removal of the patch, the number of dots on skin was counted to measure the insertion ratio. The skin was further embedded in paraffin and sectioned for hematoxylin−eosin (H&E) staining.

2.15. *In vivo biodistribution*

The *in vivo* biodistribution of SHMONs was characterized using Cy5.5-SHMONs. To establish the A375/DDP xenograft tumor model, A375/DDP cells (1×10^7 cells suspended in 100 μL of the mixture of PBS and Matrigel at a volume ratio of 1:1) were injected subcutaneously into the dorsal region of each BALB/c nude mouse. When the tumor volume reached ∼50 mm^3, A375/DDP tumor-bearing BALB/c nude mice were applied with Cy5.5-SHMONs (700 μg) *via* MN at tumor sites or tail vein injection. The fluorescence signals at different time points (2, 4, 24, 48, and 72 h post-administration) were observed using an *in vivo* imaging

system (NightOWL II LB983, Berthold Technologies, Germany). After 72 h, the mice were sacrificed and the tumors and major organs (heart, liver, spleen, lung, and kidney) were obtained for *ex vivo* fluorescence imaging.

2.16. *In vivo GSH depletion and GST inhibition*

To investigate the *in vivo* GSH depletion and GST inhibition ability of (CisPt+EA)@SHMONs [denoted as (CisPt+EA)@NPs hereafter] MN, A375/DDP tumor-bearing BALB/c nude mice (model established as mentioned in Section 2.15) were randomly divided into three groups ($n = 6$): control, (CisPt+EA)@NPs i.v., and (CisPt+EA)@NPs MN. The mice in control group received no treatment. The mice in (CisPt+EA)@NPs i.v. group were intravenously injected with (CisPt+EA)@NPs (containing 70 μg of CisPt and 38 μg of EA). The mice in group (CisPt+EA)@NPs MN were treated with MN (containing ~26 μg of CisPt and ~15 μg of EA per patch) at the tumor sites. All of the groups received treatments on Days 0, 3, and 6. The tumor sizes and body weights were recorded every other day since the first treatment. The tumor volume (V) was calculated as Eq. (1):

$$V = [a \times b^2]/2 \quad (1)$$

where a is the longest dimension of the tumor and b is the shortest dimension. On Day 2, three mice in each group were sacrificed and the tumors were collected and dissected into two parts. One part was used to detect the GSH content using a GSH and GSSG Assay Kit. The other part was used to detect the GST activity using a GST Assay Kit.

2.17. *In vivo antitumor efficacy*

The A375/DDP xenograft tumor model was established as mentioned in Section 2.15. When the tumor volume reached ~50 mm^3, the mice were randomly divided into seven groups ($n = 5$): control, CisPt i.v., blank MN, CisPt MN, CisPt@NPs MN, EA@NPs MN, and (CisPt+EA)@NPs MN. The mice in control group received no treatment. The mice in CisPt i.v. group were intravenously injected with CisPt (70 μg) in 100 μL of saline. The mice in other groups were treated with one patch of different MN (containing ~26 μg of CisPt and/or ~15 μg of EA per patch) at the tumor sites. The drug-loaded MN that prepared from CisPt, CisPt@SHMONs, EA@SHMONs, and (CisPt+EA)@SHMONs were denoted as CisPt MN, CisPt@NPs MN, EA@NPs MN, and (CisPt+EA)@NPs MN, respectively. All of the groups received treatments on Days 0, 3, and 6. The tumor sizes and body weights were recorded every other day since the first treatment. On Day 21, the mice were sacrificed and the tumors were collected, weighed, and pictured. After that, the tumors were fixed in paraformaldehyde, embedded in paraffin, and sectioned for H&E staining. To evaluate cancer cell apoptosis, the tumor sections were stained with terminal deoxynucleotidyl transferase-mediated dUTP nick end labeling (TUNEL) and cleaved caspase-3 antibody. To evaluate cancer cell proliferation, the tumor sections were stained with Ki-67 antibody.

2.18. *In vivo biosafety*

After the evaluation of the *in vivo* antitumor activity, the blood of mice was collected from the retro-orbital plexus before the mice were sacrificed. The blood samples were centrifuged at 1000×g at 4 °C for 15 min to obtain the plasma. The biochemical markers that reflect hepatic and renal function in the plasma were analyzed, including alkaline phosphatase (ALP), alanine aminotransferase (ALT), aspartate transaminase (AST), blood urea nitrogen (BUN), creatinine (CR), and uric acid (UA). The mice were dissected to obtain major organs (heart, liver, spleen, lung, and kidney) for H&E staining.

2.19. *Statistical analysis*

All data were expressed as the mean ± standard deviation (SD) unless otherwise specified. Statistical significance was analyzed using Student's t-test for two-group comparison and one-way analysis of variance (ANOVA) for multi-group comparison. $P < 0.05$ was considered to be statistically significant ($^*P < 0.05$, $^{**}P < 0.01$, and $^{***}P < 0.001$).

3. Results and discussion

3.1. *Synthesis and characterization of SHMONs*

SHMONs were synthesized *via* a conventional sol−gel process (Fig. 2A). First, MSNs, the inner core templates, were synthesized through the hydrolysis and condensation of TEOS with CTAC as the surfactant. Then, BTDS, an S−S-containing organosilane, and TEOS were co-concentrated on the surface of MSNs to obtain MSN@SMONs. Finally, the inner MSNs cores were etched by alkaline solution and the nanoparticles were aminated to obtain SHMONs.

To verify the effect of etching treatment, morphological and structural changes of the nanoparticles before and after ammonia etching were observed by TEM and SEM. The solid core−shell structure of MSN@SMONs transformed into the hollow structure of SHMONs after the etching process (Fig. 2B and C, and Supporting Information Fig. S1), which was attributed to the better resistance to alkaline etching of −Si−C− bond in the organosilica shell than that of −Si−O−Si− bond in the silica core[35]. In addition, the surface changes of nanoparticles in stepwise synthesis were also confirmed by the increasing zeta potentials (Fig. 2E). The final products SHMONs exhibited hollow structure and spherical morphology with an average particle size of approximately 70 nm (Fig. 2D). The pore structure and specific surface area of SHMONs were characterized by nitrogen absorption−desorption analysis. The results showed a typical type IV isotherm, confirming the mesoporous structure of nanoparticles with the pore size of 3.58 nm (Fig. 2G). The TGA curve showed a weight loss of ~25%, which represented the proportion of organic constituent in the chemical composition of SHMONs (Supporting Information Fig. S2). The HAADF-STEM image and EDX elemental mapping showed that C, O, Si, S, and N elements were homogeneously distributed within the structure of SHMONs (Fig. 2F). The signals of ^{13}C NMR spectrum at 2.9, 15.1, and 34.2 ppm confirmed the presence of carbon atoms from organosaline BTDS (Supporting Information Fig. S3). The signals of ^{29}Si NMR spectrum at −67.2, −75.5, −109.5, and −118.6 ppm indicated the silicon atoms with the structure of T1, T2, Q3, and Q4, respectively (Fig. 2H). The FT-IR spectrum suggested the presence of −Si−O−Si−, −Si−O−H, and −C−H− bonds (Fig. 2I). All of the results confirmed that S−S-containing organic content was successfully integrated into the framework of SHMONs.

In order to investigate the effects of S−S content on the structure, redox-response performance, and drug loading capacity

of SHMONs, a series of nanoparticles were synthesized with different volume ratios of TEOS to BTDS (5:1, 5:3, 5:6, and 5:10), and denoted as SHMONs-1, SHMONs-3, SHMONs-6, and SHMONs-10, respectively. The TGA curves showed the percentage changes of organic constituent in SHMONs with the varying feeding ratios (Supporting Information Fig. S4). According to the results of SEM and nitrogen absorption−desorption analysis, different SHMONs had similar morphology and mesoporous structure with slightly different particle sizes, surface areas, and pore diameters (Supporting Information Figs. S5 and S6, and Table S1). Among them, SHMONs-6 had the largest surface area, which was benefit for drug loading.

3.2. *Redox-responsive degradation, cellular uptake and GSH depletion of SHMONs*

We hypothesized that the S−S in the framework of SHMONs would be broken in the presence of high level of GSH in cancer cells, which could promote the degradation of nanoparticles and the intracellular GSH depletion. Firstly, we verified the redox-responsive break of the S−S *via* Ellman's test. The S−S in the framework of SHMONs can be reduced by reducing agents like GSH and DTT, and generated sulfydryl groups (−SH). The Ellman's reagent, DTNB, can react with −SH to form TNB^{2-}, which has strong absorbance at 412 nm[36]. As a control, HMONs that did not contain S−S were synthesized (Supporting Information Fig. S7). According to the results of UV−Vis spectrometry, the Ellman's reagent showed almost no absorbance after treated with HMONs that were pre-incubated with DTT, while significant absorbance was observed for the samples treated with SHMONs (Fig. 3A and B). Moreover, the absorbance values of SHMONs group increased along with the increasing incubation time, which indicated more −SH was generated over time. In addition, SHMONs prepared with different feeding ratios showed different absorbances, and thereinto, SHMONs-6 exhibited better −SH-generating ability (Supporting Information Fig. S8). Next, we investigated whether the break of S−S would accelerate the degradation of SHMONs. The morphology of SHMONs incubated in PBS with or without 10 mmol/L of GSH for 1, 4, and 7 days was observed by TEM. As shown in TEM images (Fig. 3D), broken fringes, collapsed frameworks, and indistinct degradation fragments were observed for the nanoparticles treated with GSH. As a contrast, the nanoparticles treated with PBS for up to 7 days still had intact structures and outlines with clear background. These results demonstrated that SHMONs could be degraded in the intracellular reducing environment. In view of the fact that common silica-based materials degraded slowly *in vivo* and might induce long-term toxicity, this property greatly improved the biocompatibility of SHMONs[37,38].

When SHMONs arrived at tumor tissue, they could be internalized by tumor cells. The cellular uptake of SHMONs was studied by flow cytometry and CLSM using FITC-SHMONs (Fig. 3C and E). The results show that the uptake of nanoparticles by A375/DDP cells was time-dependent and almost reached saturation after incubation for 1 h. Once internalized by cancer cells, SHMONs were supposed to be degraded in response to high level of intracellular GSH and consume GSH at the same time. We measured the GSH levels of A375/DDP cells after different treatments (Fig. 3F). Significant decrease of GSH level was observed in cells treated with BSO (a GSH synthesis inhibitor) and SHMONs, which indicated that SHMONs could induce GSH depletion in cancer cells. As a negative control, HMONs treatment only caused slight decrease of GSH level, which might be due to the moderate increase of cellular oxidative stress triggered by the size effect of nanoparticles[39,40]. In addition, GSH depletion would disturb redox homeostasis in cells, which can be reflected in the reactive oxygen species (ROS) level[41]. We used a ROS probe, DCFH-DA, to detect the intracellular ROS in A375/DDP cells (Fig. 3G). In accordance with the results of GSH levels, cells treated with BSO or SHMONs showed strong signals of DCFH, indicating higher ROS levels than untreated cells.

All of these results confirm that SHMONs could be degraded in the reducing environment and induce GSH depletion in cancer cells, which were potential biocompatible nanocarriers that could resist GSH-mediated cellular detoxification for CisPt delivery.

3.3. *In vitro drug release and CisPt resistance reversal of (CisPt+EA)@SHMONs*

CisPt and EA were successfully loaded into SHMONs, as confirmed by the characteristic peaks in FT-IR and decreased surface area (Supporting Information Fig. S9 and Table S2). The drug loading contents of different SHMONs were shown in Supporting Information Table S3. SHMONs-6 had higher drug loading capacity than other nanoparticles, which were probably attributed to the higher surface area (Supporting Information Table S1). Since SHMONs-6 had superior redox-responsive degradability and drug loading capacity, it was chosen and used for the following experiments. In order to investigate whether the redox-responsive degradation of SHMONs would promote drug release, CisPt release was tested in the conditions with or without reducing agent. The CisPt contents were quantified by ICP-AES. In PBS without reducing agent, the released CisPt in the medium could not be detected by ICP-AES because the concentrations of Pt were lower than limit of detection, which indicated pretty lower drug release. However, after the addition of reducing agent, about 11.6% of CisPt was released from the nanoparticles after 7 days (Fig. 4A). This redox-responsive drug release property suggested that the redox-responsive degradation of SHMONs might facilitate drug release from the nanoparticles, which is beneficial for precise drug delivery in the high redox tumor environment. EA could not be quantified by high performance liquid chromatograph (HPLC) in the presence of reducing agent because it would react with the reducing agent[42,43], so only the release in PBS without reducing agent was detected (Supporting Information Fig. S10).

To evaluate the *in vitro* antitumor activity and drug resistance reversal of (CisPt+EA)@SHMONs, cytotoxicity assays were tested on A375 and A375/DDP cells. Before that, we tested the cytotoxicity of drug-free SHMONs. The results show that SHMONs did not present obvious cytotoxicity to both cells, suggesting the good biocompatibility of the nanoparticles (Supporting Information Fig. S11). A slightly higher toxicity was observed in A375/DDP cells than in A375 cells, which might be attributed to the higher sensitivity of drug-resistant cells to GSH dyshomeostasis caused by SHMONs than drug-sensitive cells[44]. In A375 cells, free CisPt showed significant cytotoxicity with an IC_{50} value of 0.58 μg/mL (Fig. 4B), which was better than CisPt@SHMONs. The nano-formulations did not show significant superiority compared with free drugs. After the addition of EA, the antitumor activities of CisPt were moderately enhanced for both free drugs and nanoformulations. In A375/DDP cells, the toxicity of free CisPt was much lower than drug-sensitive cells with an IC_{50} value of 13.05 μg/mL (Fig. 4C). By contrast, CisPt@SHMONs and (CisPt+EA)@SHMONs exhibited better antitumor activities than CisPt,

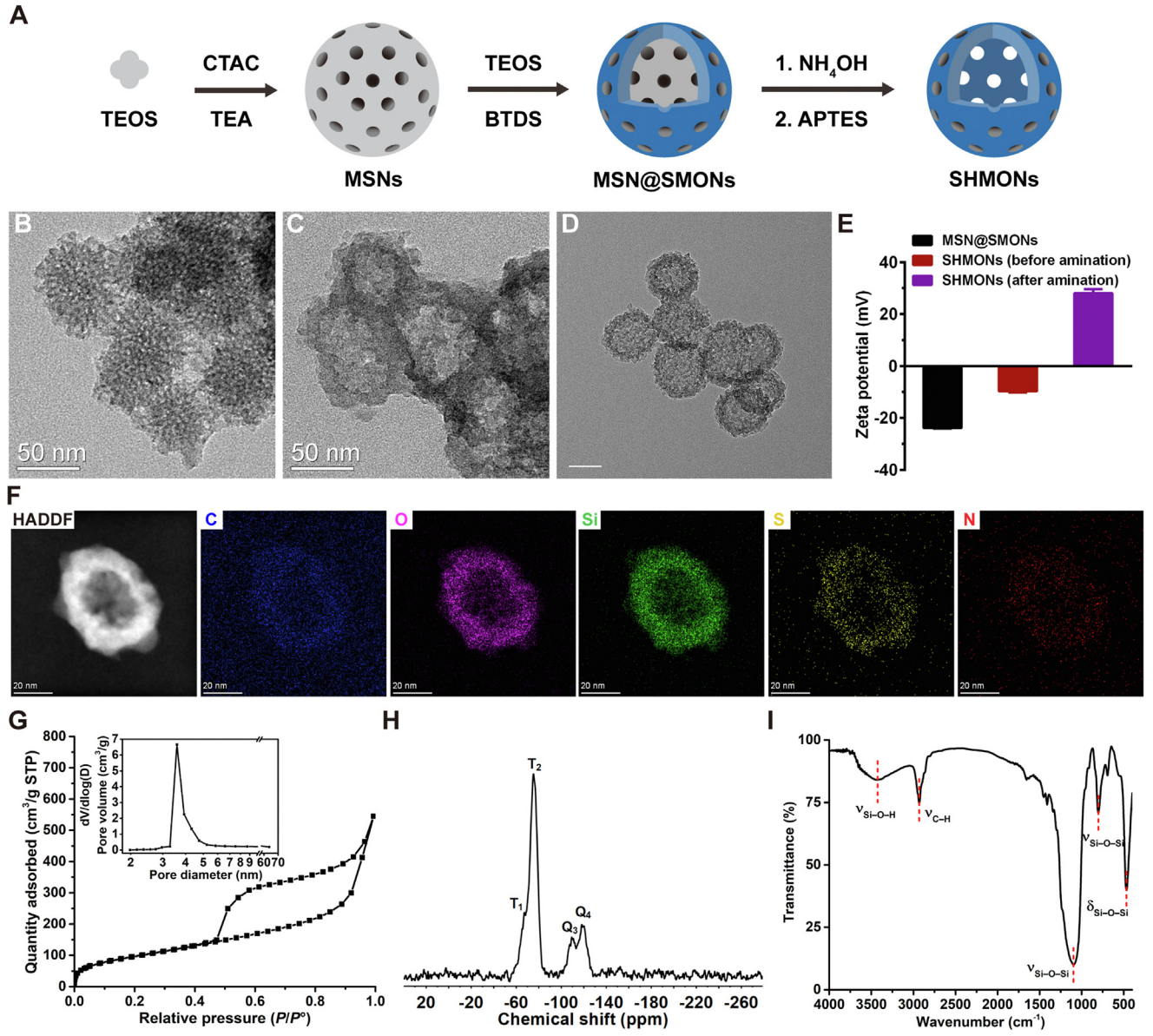

Figure 2 Synthesis and characterization of SHMONs. (A) Schematic illustration of the synthetic process of SHMONs. TEM images of (B) MSN@SMONs (before etching) and (C) SHMONs (after etching). (D) TEM image of the final product SHMONs. Scale bar = 50 nm. (E) Zeta potentials of MSN@SMONs, SHMONs (before amination), and SHMONs (after amination). Data are presented as mean ± SD (n = 3). (F) HAADF-STEM image of SHMONs and corresponding element mapping images of C, O, Si, S, and N. (G) Nitrogen absorption−desorption isotherm and pore diameter distribution of SHMONs. (H) ^{29}Si NMR spectrum of SHMONs. (I) FT-IR spectrum of SHMONs.

which indicated the important roles of SHMONs and EA. In accordance with the results of cytotoxicity, cell apoptosis assay also indicated that (CisPt+EA)@SHMONs had the strongest capability of apoptosis-inducing effect in A375/DDP cells (Fig. 4D).

In order to investigate the antitumor mechanism of (CisPt+EA)@SHMONs, we firstly measured the cellular Pt accumulation of free drugs and nano-formulations. As shown in Fig. 4E, the accumulations of Pt in A375/DDP cells after incubation with free CisPt were significantly lower than those in A375 cells. By contrast, the cellular uptake of Pt from (CisPt+EA)@SHMONs was similar for both cells. These results suggested that SHMONs could help CisPt to bypass the CTR1 pathway and improve the accumulation of CisPt in drug-resistant cells. After internalization by cells, CisPt can interact with DNA and form Pt-DNA adducts, which further induces cell apoptosis. However, the defense system of cells can hinder this process, especially in drug-resistant cancer cells. The intracellular GSH can be bound with CisPt under the catalysis of GST, forming conjugates that are further extruded by cancer cells. This drug detoxification process can significantly weaken the therapeutic efficacy of CisPt and develop drug resistance. We determined the contents of Pt-DNA adducts in A375/DDP cells after different treatments (Fig. 4F). The addition of BSO increased the contents of Pt-DNA adducts as compared with CisPt alone, which demonstrated that cellular GSH depletion could improve the efficacy of CisPt. Similar improvement was observed for CisPt@SHMONs. Combined with the results that SHMONs

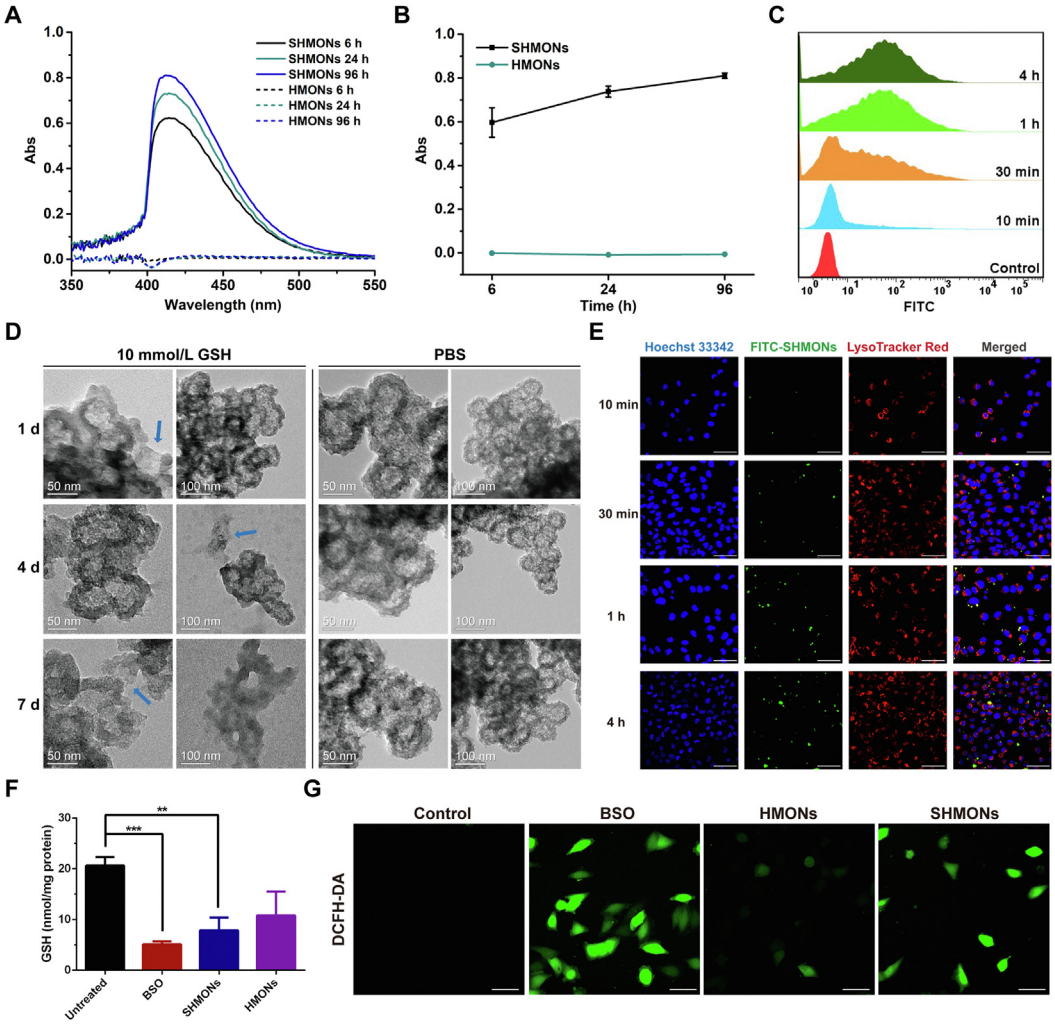

Figure 3 Redox-responsive degradation, cellular uptake and GSH depletion of SHMONs. (A) UV−vis absorption spectra of DTNB solutions after incubation with SHMONs or HMONs for different time and (B) the corresponding absorbances at 412 nm. Data are presented as mean ± SD ($n = 3$). (C) Flow cytometry analysis of A375/DDP cells after incubation with FITC-SHMONs (40 μg/mL) for different duration (10 min, 30 min, 1 h, and 4 h). (D) TEM images of SHMONs (0.1 mg/mL) after incubation in PBS with or without 10 mmol/L of GSH for different duration (1, 4, and 7 days). (E) CLSM images of A375/DDP cells stained with Hoechst 33342 and LysoTracker Red DND-99 after incubation with FITC-SHMONs (40 μg/mL) for different duration (10 min, 30 min, 1 h, and 4 h). Scale bar = 50 μm. (F) GSH levels of A375/DDP cells after incubation with BSO (200 μmol/L), SHMONs (120 μg/mL), and HMONs (120 μg/mL) for 6 h. Data are presented as mean ± SD ($n = 3$); $^{**}P < 0.01$, $^{***}P < 0.001$. (G) CLSM images of A375/DDP cells incubated with DCFH-DA for the observation of ROS generation after incubation with BSO (200 μmol/L), SHMONs (60 μg/mL), and HMONs (60 μg/mL) for 6 h. Scale bar = 50 μm.

could efficiently consumed GSH (Fig. 3F), we could deduce that CisPt@SHMONs prevented GSH detoxification of CisPt by consuming GSH and consequently increased the contents of Pt-DNA adducts. The addition of EA also exhibited positive promotion on the formation of Pt-DNA adducts. To investigate the effect of GST on the efficacy of CisPt, we measured the cellular GST activity after different treatments (Fig. 4G). GST activity in A375/DDP cells was higher than that in A375 cells. Moreover, the GST activity in A375/DDP cells increased after incubation with free CisPt. This suggests that CisPt-resistant cells enhanced their detoxification of CisPt probably by upregulating GST activity. By comparison, the addition of EA could significantly inhibit the GST activity and then weaken GSH detoxification, which could increase the contents of Pt-DNA adducts and improve the toxicity of CisPt. The above results demonstrate that (CisPt+EA)@SHMONs could effectively kill A375/DDP cells and reverse their CisPt resistance based on the "pincer movement" strategy of simultaneous GSH depletion and GST inhibition.

3.4. *Preparation and characterization of MN patch*

For the purpose of achieving effective delivery to melanoma, the (CisPt+EA)@SHMONs were loaded into dissolving MN (Fig. 5A). MN patch is an array of micron-size needles with lengths from tens of to thousands of micrometers, which can pierce the stratum corneum and even the epidermis to achieve high-efficient transdermal drug delivery[45]. Taking advantage of the superior targeting efficiency, MN has been widely used for treating superficial cancers, including melanoma[46,47], breast cancer[48], osteosarcoma[49], and pharyngeal squamous cell carcinoma[50]. In this work, HA was chosen as the matrix material to prepare

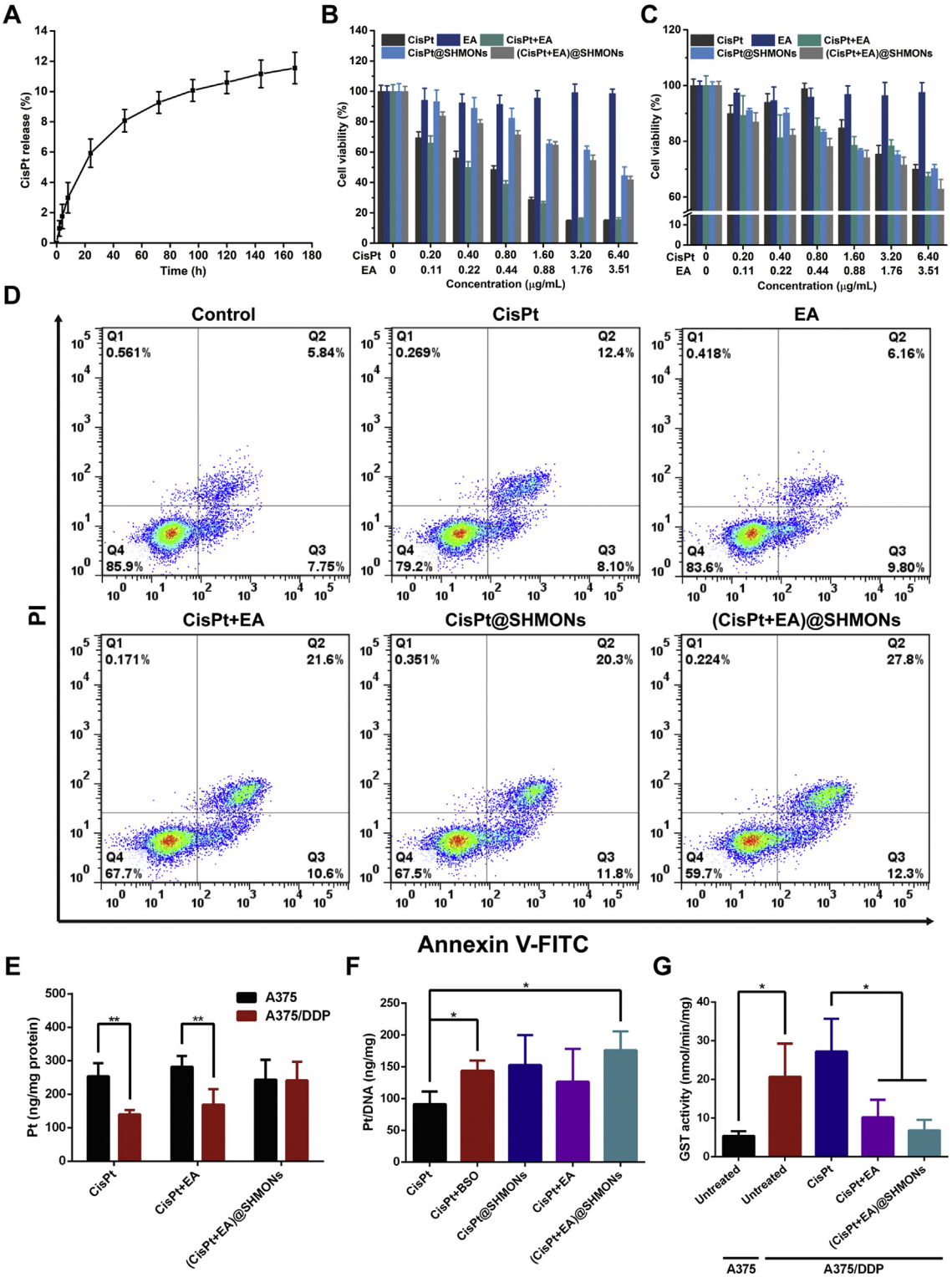

Figure 4 *In vitro* drug release and CisPt resistance reversal of (CisPt+EA)@SHMONs. (A) Drug release profile of CisPt from (CisPt+EA)@SHMONs in PBS (pH 7.4) containing 10 mmol/L of TCEP·HCl. Data are presented as mean ± SD ($n = 3$). Cytotoxicity assays of different treatments on (B) A375 cells and (C) A375/DDP cells for 48 h. Data are presented as mean ± SD ($n = 4$). (D) Cell apoptosis assays of different treatments on A375/DDP cells at a CisPt concentration of 6.4 μg/mL for 48 h. (E) The Pt uptake of A375 cells and A375/DDP cells after different treatments at a CisPt concentration of 6.4 μg/mL for 4 h. Data are presented as mean ± SD ($n = 3$); $^{**}P < 0.01$. (F) The Pt content in the genomic DNA of A375/DDP cells after different treatments at a CisPt concentration of 6.4 μg/mL for 4 h. Data are presented as mean ± SD ($n = 3$); $^{*}P < 0.05$. (G) GST activity of A375 cells and A375/DDP cells after different treatments at a CisPt concentration of 6.4 μg/mL for 4 h. Data are presented as mean ± SD ($n = 3$); $^{*}P < 0.05$.

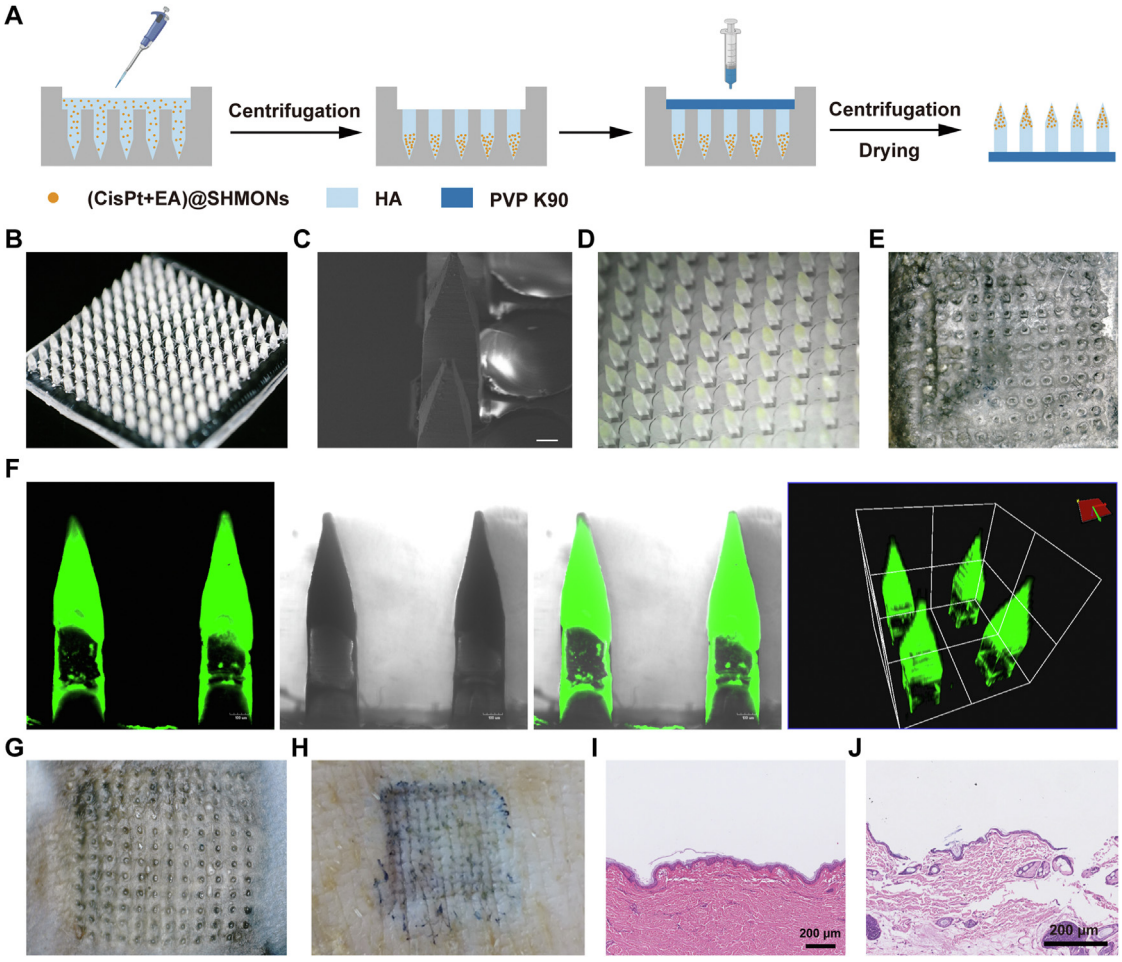

Figure 5 Characterization of (CisPt+EA)@SHMONs-loaded MN. (A) Schematic illustration of the preparation process of MN. (B) Photograph of a 12 × 12-array MN patch. (C) SEM image of the MN. Scale bar = 100 μm. (D) Magnified photograph of (CisPt+EA)@SHMONs-loaded MN. (E) Photograph of the MN patch removed from rat skin. (F) CLSM images of FITC-SHMONs-loaded MN and the corresponding 3D reconstruction image. Scale bar = 100 μm. Photographs of the (G) rat and (H) porcine skin after MN insertion and the corresponding H&E-stained tissue sections from (I) rat and (J) porcine skin.

nanoparticles-loaded MN due to its good dissolving property and biocompatibility[51,52]. The MN was arranged in a 12 × 12-array on a backing layer made of polyvinylpyrrolidone K90 (PVP K90) to form a patch (Fig. 5B). The SEM image showed the microscopic morphology of MN with a height of ~1200 μm and a width of ~300 μm (Fig. 5C). In order to characterize the distribution of nanoparticles in MN, we used FITC-SHMONs to prepare MN and observed using CLSM. As shown in Fig. 5F, most of the nanoparticles were homogeneously distributed in the needle tips of MN, which favored deeper penetration of nanoparticles after skin puncture. Similar distribution of (CisPt+EA)@SHMONs in MN was also confirmed from the yellow color of CisPt-loaded nanoparticles in the digital photo (Fig. 5D). To evaluate the skin puncture ability of MN, the *ex vivo* skin from SD rat and pig was used. The MN patch was pressed onto skin for 2 min and then remained for another 5 min. After removal of the patch from skin, it was found that almost all needles on the patch were dissolved (Fig. 5E). Fast dissolution of MN was beneficial for the release and delivery of the loaded nanoparticles and improved the convenience of administration. As shown in Supporting Information Fig. S12, almost all the nanoparticles could be released from MN within 5 min. Moreover, the morphology of the nanoparticles did not exhibit significant change after release from MN, indicating their good stability (Supporting Information Fig. S13). After administration, the micro-holes on the skin created by MN could be clearly observed, which showed that almost all needles on the patch were successfully inserted into the skin (Fig. 5G and H). The H&E-stained skin tissue section also confirmed the formation of micro-holes on skin after MN insertion (Fig. 5I and J). These results suggested the good skin puncture ability of (CisPt+EA)@SHMONs-loaded MN, which provided possibility for efficient drug delivery to superficial tumor.

3.5. *In vivo biodistribution, GSH depletion, and GST inhibition*

In order to evaluate the tumor accumulation and retention ability of nanoparticles administrated by MN, we detected the *in vivo* biodistribution of Cy5.5-SHMONs delivered by MN on A375/DDP tumor-bearing nude mice. As a comparison, mice treated by i.v. injection of Cy5.5-SHMONs were also tested. The MN group showed strong fluorescence signals at tumor site after administration and the fluorescence signals could be detected even at 72 h (Fig. 6A). After the mouse was sacrificed, the tumor and main organs were taken out for fluorescence imaging. The tumor from

MN group exhibited the strongest fluorescence, which was much higher than the fluorescence of main organs including liver. This fact suggested that the nanoparticles administrated by MN could be accumulated in the tumor site for pretty long time and less distributed in other organs. In contrast, very weak fluorescence signal of Cy5.5-SHMONs was detected at the tumor site of mouse administrated by i.v. injection, probably owing to their poor targeting ability and the clearance by reticuloendothelial system[53,54]. These results indicate that MN could be an excellent approach for nanoparticle delivery, with better superficial tumor accumulation and retention ability than i.v. injection.

Subsequently, we evaluated the *in vivo* GSH depletion and GST inhibition ability. The A375/DDP tumor-bearing nude mice were administrated with one patch of CisPt+EA)@NPs MN at the tumor sites or intravenously injected with (CisPt+EA)@NPs. After 48 h, the mice were sacrificed and the tumors were extracted for detecting GSH content and GST activity. Compared with the control group, the GSH levels in the tumors of mice treated with i.v. injection slightly decreased, which might be attributed to the limited accumulation of (CisPt+EA)@NPs in tumors (Fig. 6B). By contrast, the GSH levels were significantly reduced in the MN group, due to its higher tumor accumulation and GSH-depleting ability. Similar results were observed for GST activity, indicating strong GST inhibiting effect of EA in (CisPt+EA)@NPs MN group (Fig. 6C). During 14 days of observation, the tumor growth of mice in (CisPt+EA)@NPs MN group was better suppressed compared with those in control group and (CisPt+EA)@NPs i.v. group (Supporting Information Fig. S14). All of these results demonstrate that (CisPt+EA)@NPs delivered by MN could effectively deplete GSH and inhibit GST activity in CisPt-resistant tumors, which successfully gathered two pieces of the "pincer" for executing "pincer movement" strategy.

3.6. *In vivo antitumor efficacy and biosafety*

The antitumor efficacy of (CisPt+EA)@NPs MN was evaluated on A375/DDP tumor-bearing nude mice (Fig. 7A). During the observation period of 20 days, the tumors in control group grew rapidly, which represented the natural progression of CisPt-resistant melanomas (Fig. 7B). Compared with control group, the tumor growth in CisPt i.v., blank MN, CisPt MN, CisPt@NPs MN, and EA@NPs MN groups were suppressed to different degrees. It is worth noting that the dose of CisPt *via* intravenous injection was ~2.5 times higher than those in MN. Although similar suppression effects were observed, the application of MN could increase the drug efficacy and decrease the drug dose. Moreover, the body weights of mice in CisPt i.v. group reduced slightly during the observation period (Fig. 7C), suggesting potential toxicity of CisPt *via* systemic administration. In addition, the moderate suppression effect on tumor growth in blank MN group might result from possible tumor tissue injury by pressure force during administration. (CisPt+EA)@NPs MN showed the most effective suppression on tumor growth compared with other groups. Similar results were also observed from the tumor images (Fig. 7D) and tumor weights (Supporting Information Fig. S15). To further investigate the antitumor effects at tissue level and

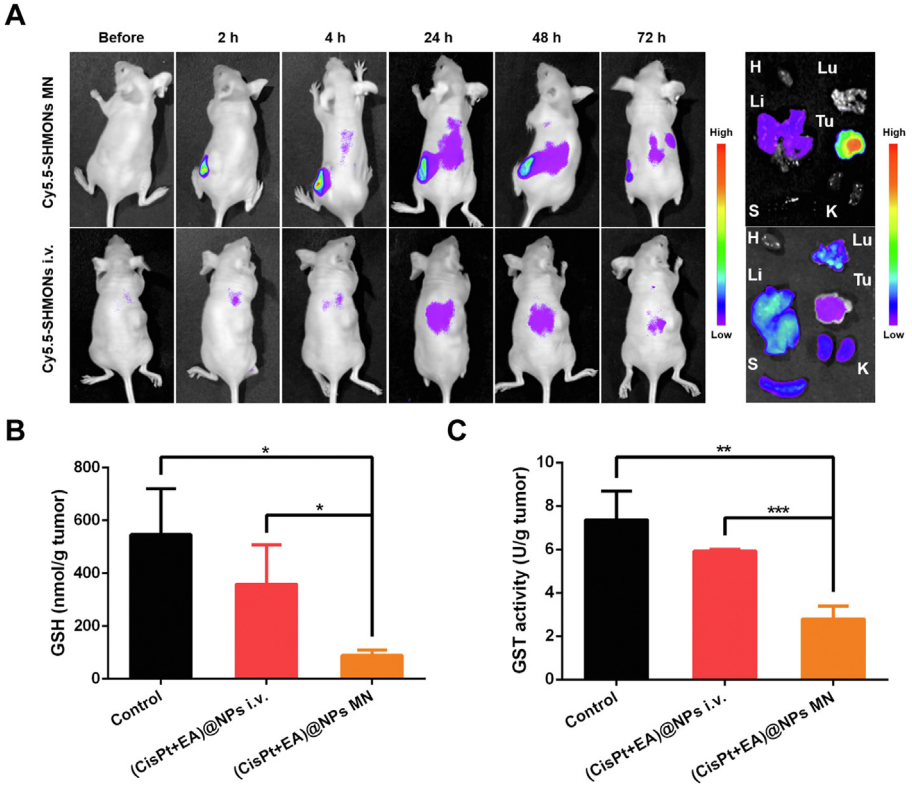

Figure 6 *In vivo* biodistribution, GSH depletion, and GST inhibition. (A) Biodistribution of Cy5.5-SHMONs in A375/DDP tumor-bearing nude mice administrated by MN and i.v. injection. (B) GSH levels in the tumor tissues of the mice after different treatments. Data are presented as mean ± SD ($n = 3$); *$P < 0.05$. (C) GST activity in the tumor tissues of the mice after different treatments. Data are presented as mean ± SD ($n = 3$); **$P < 0.01$, ***$P < 0.001$.

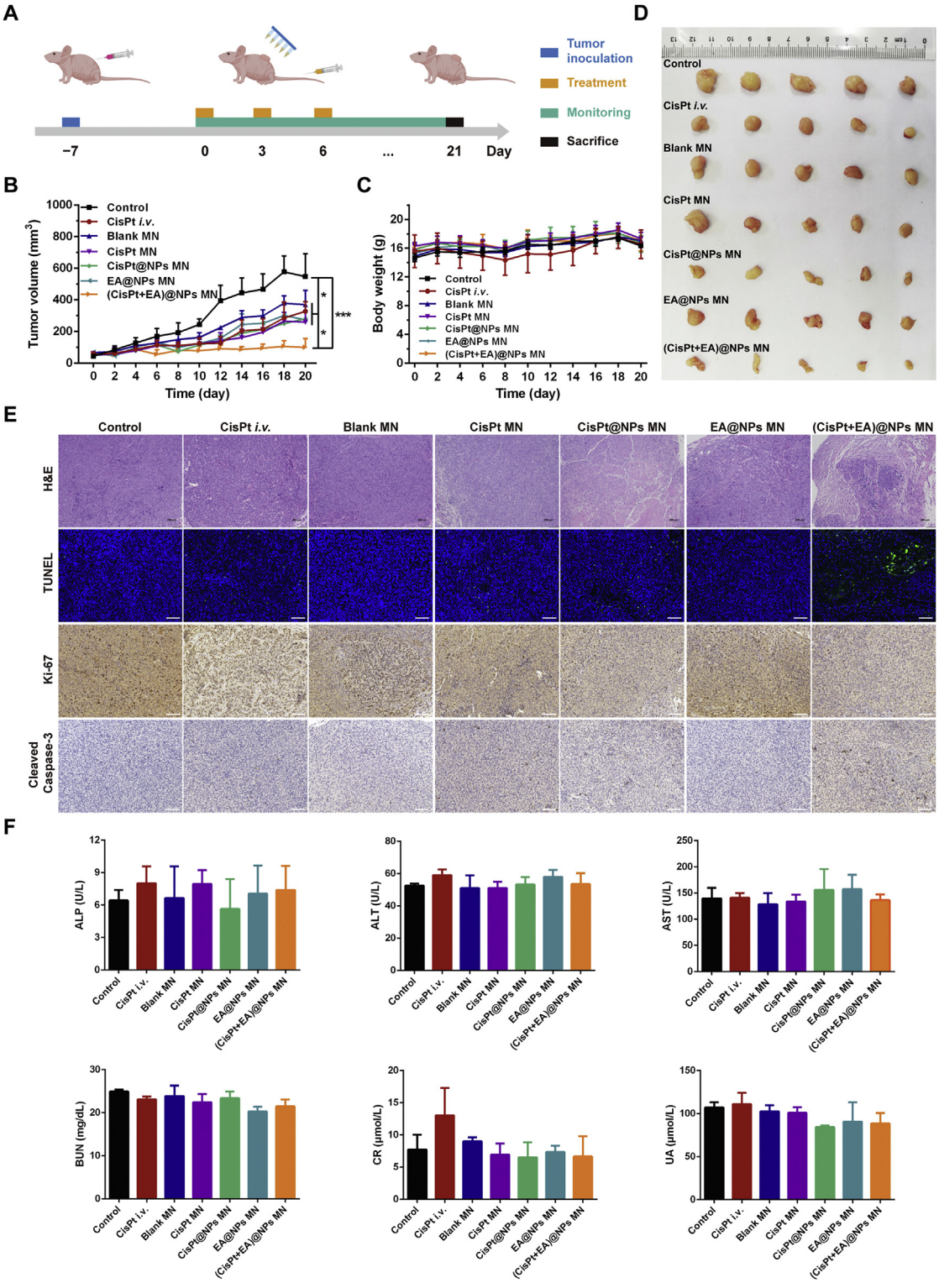

Figure 7 *In vivo* antitumor efficacy and biosafety evaluation. (A) Schematic illustration of the establishment and treatment of A375/DDP tumor-bearing nude mice model. (B) Tumor growth curves of tumor-bearing mice after different treatments. Data are presented as mean ± SD ($n = 5$); $^{*}P < 0.05$, $^{***}P < 0.001$. (C) Body weight changes of the tumor-bearing mice after different treatments. Data are presented as mean ± SD ($n = 5$). (D) Photographs of tumors extracted from the tumor-bearing mice after different treatments. (E) H&E staining, TUNEL assay, immunohistochemical analysis of Ki-67, and cleaved caspase-3 of tumor sections from the tumor-bearing mice after different treatments. Scale bar = 200 μm for images of H&E. Scale bar = 100 μm for images of TUNEL, Ki-67, and cleaved caspase-3. (F) Biochemical analysis of plasma collected from the tumor-bearing mice after different treatments. Data are presented as mean ± SD ($n = 3$).

cellular level, histopathological analysis was conducted on the extracted tumors (Fig. 7E). After H&E staining, obvious nucleus shrinkage and fragmentation were observed in the tumor section from the (CisPt+EA)@NPs MN group, indicating extensive cell death. Additionally, the results of TUNEL assay show more apoptotic cells existed in the tumor of mice treated with (CisPt+EA)@NPs MN. Likewise, more positive cells in immunohistochemical analysis for cleaved caspase-3 indicated enhanced cell apoptosis level in the tumor of mice treated with (CisPt+EA)@NPs MN. Meanwhile, much less Ki-67-positive cells in the (CisPt+EA)@NPs MN group suggested stronger suppression on tumor cell proliferation. Taken together, these results demonstrate that (CisPt+EA)@NPs MN based on the "pincer movement" strategy could effectively induce tumor cell apoptosis and suppress tumor growth, exhibiting much better therapeutic efficacy than traditional chemotherapy against CisPt-resistant tumor.

In addition, we evaluated the biosafety of different formulations. The blood of mice was collected for blood biochemical analysis after tumor monitoring. The levels of ALP, ALT, AST, BUN, CR, and UA in plasma were measured for evaluating the hepatic and renal function (Fig. 7F). A slightly higher CR level in CisPt i.v. group suggested that systematic administration of CisPt probably cause damage to kidney. No obvious abnormal biomarkers were detected in other groups, indicating their low hepatotoxicity and nephrotoxicity. The tissue sections of major organs (heart, liver, spleen, lung, and kidney) were stained with H&E for histological examination (Supporting Information Fig. S16). No obvious tissue injuries were observed for all of the groups. CisPt is known for its nephrotoxicity and hepatotoxicity in clinical applications[55]. Although only slightly decreased body weight and increased CR level were observed in CisPt i.v. group at the specific dose in this study, the potential toxicity of CisPt is still a worrying problem. Therefore, (CisPt+EA)@NPs MN could be an excellent candidate for reversing CisPt resistance of tumors while not inducing significant toxicity at a lower dose.

4. Conclusions

In summary, a redox-responsive nanomedicine based on CisPt- and EA-loaded SHMONs was successfully prepared and optimized for reversing drug resistance in CisPt-mediated cancer chemotherapy. At the tumor microenvironment of high GSH level, the S−S-bridged SHMONs could be degraded and further promoted drug release. The *in vitro* cell experiments showed that the intracellular GSH was consumed by SHMONs and the GST activity was inhibited by the released EA. This "pincer movement" of the nanomedicine effectively promoted the formation of Pt-DNA adducts and enhanced the cytotoxicity and apoptosis-inducing ability of CisPt. After being integrated into the MN, the nanomedicine suppressed tumor growth on an A375/DDP melanoma model without obvious systemic toxicity. This nanomedicine provides a valuable paradigm for overcoming CisPt resistance by simultaneous GSH depletion and GST inhibition and extends the application of organosilica hybrid nanomaterials in biomedical field.

Acknowledgments

This work was financially supported by the National Natural Science Foundation of China (No. 81803466), the Natural Science Foundation of Guangdong Province (No. 2018A030310095, China), and the Key Areas Research and Development Program of Guangdong Province (No. 2019B020204002, China).

Author contributions

Boyi Niu, Yixian Zhou, Guilan Quan, and Xin Pan designed the research. Boyi Niu, Yixian Zhou, Kaixin Liao, Ting Wen, and Sixian Lao performed the experiments. Boyi Niu and Yixian Zhou wrote the manuscript. Guilan Quan, Xin Pan, and Chuanbin Wu revised the manuscript. Guilan Quan and Chuanbin Wu provided the funding. All authors have read and approved the final manuscript.

Conflicts of interest

The authors have no conflicts of interest to declare.

Appendix A. Supporting information

Supporting data to this article can be found online at https://doi.org/10.1016/j.apsb.2021.10.013.

References

1. Lheureux S, Braunstein M, Oza AM. Epithelial ovarian cancer: evolution of management in the era of precision medicine. *CA Cancer J Clin* 2019;**69**:280−304.
2. Chow LQM. Head and neck cancer. *N Engl J Med* 2020;**382**:60−72.
3. Fennell DA, Summers Y, Cadranel J, Benepal T, Christoph DC, Lal R, et al. Cisplatin in the modern era: the backbone of first-line chemotherapy for non-small cell lung cancer. *Cancer Treat Rev* 2016;**44**:42−50.
4. Garbe C, Eigentler TK, Keilholz U, Hauschild A, Kirkwood JM. Systematic review of medical treatment in melanoma: current status and future prospects. *Oncol* 2011;**16**:5−24.
5. Shen DW, Pouliot LM, Hall MD, Gottesman MM. Cisplatin Resistance: a cellular self-defense mechanism resulting from multiple epigenetic and genetic changes. *Pharmacol Rev* 2012;**64**:706−21.
6. Galluzzi L, Senovilla L, Vitale I, Michels J, Martins I, Kepp O, et al. Molecular mechanisms of cisplatin resistance. *Oncogene* 2012;**31**:1869−83.
7. Kelland LR. Preclinical perspectives on platinum resistance. *Drugs* 2000;**59**:1−8.
8. Duan M, Ulibarri J, Liu KJ, Mao P. Role of nucleotide excision repair in cisplatin resistance. *Int J Mol Sci* 2020;**21**:9248.
9. Lobo J, Jerónimo C, Henrique R. Cisplatin resistance in testicular germ cell tumors: current challenges from various perspectives. *Cancers* 2020;**12**:1601.
10. Chen G, Yang Y, Xu Q, Ling M, Lin H, Ma W, et al. Self-amplification of tumor oxidative stress with degradable metallic complexes for synergistic cascade tumor therapy. *Nano Lett* 2020;**20**:8141−50.
11. Kasherman Y, Sturup S, Gibson D. Is glutathione the major cellular target of cisplatin? A study of the interactions of cisplatin with cancer cell extracts. *J Med Chem* 2009;**52**:4319−28.
12. Mistry P, Kelland LR, Abel G, Sidhar S, Harrap KR. The relationships between glutathione, glutathione-*S*-transferase and cytotoxicity of platinum drugs and melphalan in eight human ovarian carcinoma cell lines. *Br J Cancer* 1991;**64**:215−20.
13. Pljesa-Ercegovac M, Savic-Radojevic A, Matic M, Coric V, Djukic T, Radic T, et al. Glutathione transferases: potential targets to overcome chemoresistance in solid tumors. *Int J Mol Sci* 2018;**19**:3785.
14. Allocati N, Masulli M, Di Ilio C, Federici L. Glutathione transferases: substrates, inihibitors and pro-drugs in cancer and neurodegenerative diseases. *Oncogenesis* 2018;**7**:8.
15. Li S, Li C, Jin S, Liu J, Xue X, Eltahan AS, et al. Overcoming resistance to cisplatin by inhibition of glutathione *S*-transferases

(GSTs) with ethacraplatin micelles *in vitro* and *in vivo*. *Biomaterials* 2017;**144**:119−29.
16. Yang Y, Yu Y, Chen H, Meng X, Ma W, Yu M, et al. Illuminating platinum transportation while maximizing therapeutic efficacy by gold nanoclusters *via* simultaneous near-infrared-I/II imaging and glutathione scavenging. *ACS Nano* 2020;**14**:13536−47.
17. Rocha CRR, Garcia CCM, Vieira DB, Quinet A, de Andrade-Lima LC, Munford V, et al. Glutathione depletion sensitizes cisplatin- and temozolomide-resistant glioma cells *in vitro* and *in vivo*. *Cell Death Dis* 2014;**5**:e1505.
18. Yang LH, Zhao HB, Yin XQ, Liang H, Zheng Z, Shen Q, et al. Exploring cisplatin resistance in ovarian cancer through integrated bioinformatics approach and overcoming chemoresistance with sanguinarine. *Am J Transl Res* 2020;**12**:923.
19. Xu Y, Han X, Li Y, Min H, Zhao X, Zhang Y, et al. Sulforaphane mediates glutathione depletion *via* polymeric nanoparticles to restore cisplatin chemosensitivity. *ACS Nano* 2019;**13**:13445−55.
20. Brien ML, Vulevic B, Freer S, Boyd J, Shen H, Tew KD. Glutathione peptidomimetic drug modulator of multidrug resistance-associated protein. *J Pharmacol Exp Ther* 1999;**291**:1348.
21. Liu X, Wang W, Yin Y, Li M, Li H, Xiang H, et al. A high-throughput drug screen identifies auranofin as a potential sensitizer of cisplatin in small cell lung cancer. *Invest New Drugs* 2019;**37**:1166−76.
22. Godwin AK, Meister A, Dwyer PJ, Huang CS, Hamilton TC, Anderson ME. High resistance to cisplatin in human ovarian cancer cell lines is associated with marked increase of glutathione synthesis. *Proc Natl Acad Sci U S A* 1992;**89**:3070.
23. Bansal A, Simon MC. Glutathione metabolism in cancer progression and treatment resistance. *J Cell Biol* 2018;**217**:2291−8.
24. Ishida S, Lee J, Thiele DJ, Herskowitz I. Uptake of the anticancer drug cisplatin mediated by the copper transporter Ctr1 in yeast and mammals. *Proc Natl Acad Sci U S A* 2002;**99**:14298−302.
25. Shanbhag VC, Gudekar N, Jasmer K, Papageorgiou C, Singh K, Petris MJ. Copper metabolism as a unique vulnerability in cancer. *Biochim Biophys Acta Mol Cell Res* 2021;**1868**:118893.
26. Ishida S, McCormick F, Smith-McCune K, Hanahan D. Enhancing Tumor-specific uptake of the anticancer drug cisplatin with a copper chelator. *Cancer Cell* 2010;**17**:574−83.
27. Cho K, Wang X, Nie S, Chen Z, Shin DM. Therapeutic nanoparticles for drug delivery in cancer. *Clin Cancer Res* 2008;**14**:1310.
28. Chen Q, Yang Y, Lin X, Ma W, Chen G, Li W, et al. Platinum(IV) prodrugs with long lipid chains for drug delivery and overcoming cisplatin resistance. *Chem Commun* 2018;**54**:5369−72.
29. Ling X, Chen X, Riddell IA, Tao W, Wang J, Hollett G, et al. Glutathione-scavenging poly(disulfide amide) nanoparticles for the effective delivery of Pt(IV) prodrugs and reversal of cisplatin resistance. *Nano Lett* 2018;**18**:4618−25.
30. Han Y, Yin W, Li J, Zhao H, Zha Z, Ke W, et al. Intracellular glutathione-depleting polymeric micelles for cisplatin prodrug delivery to overcome cisplatin resistance of cancers. *J Control Release* 2018;**273**:30−9.
31. Zhang J, Zhao B, Chen S, Wang Y, Zhang Y, Wang Y, et al. Near-infrared light irradiation induced mild hyperthermia enhances glutathione depletion and DNA interstrand cross-link formation for efficient chemotherapy. *ACS Nano* 2020;**14**:14831−45.
32. Zhou Y, Quan G, Wu Q, Zhang X, Niu B, Wu B, et al. Mesoporous silica nanoparticles for drug and gene delivery. *Acta Pharm Sin B* 2018;**8**:165−77.
33. Chen Y, Shi J. Chemistry of mesoporous organosilica in nanotechnology: molecularly organic−inorganic hybridization into frameworks. *Adv Mater* 2016;**28**:3235−72.
34. Huang P, Qian X, Chen Y, Yu L, Lin H, Wang L, et al. Metalloporphyrin-encapsulated biodegradable nanosystems for highly efficient magnetic resonance imaging-guided sonodynamic cancer therapy. *J Am Chem Soc* 2017;**139**:1275−84.
35. Huang P, Chen Y, Lin H, Yu L, Zhang L, Wang L, et al. Molecularly organic/inorganic hybrid hollow mesoporous organosilica nanocapsules with tumor-specific biodegradability and enhanced chemotherapeutic functionality. *Biomaterials* 2017;**125**:23−37.
36. Riener CK, Kada G, Gruber HJ. Quick measurement of protein sulfhydryls with Ellman's reagent and with 4,4′-dithiodipyridine. *Anal Bioanal Chem* 2002;**373**:266−76.
37. Croissant JG, Fatieiev Y, Khashab NM. Degradability and clearance of silicon, organosilica, silsesquioxane, silica mixed oxide, and mesoporous silica nanoparticles. *Adv Mater* 2017;**29**:1604634.
38. Liu X, Yang Y, Ling M, Sun R, Zhu M, Chen J, et al. Near-infrared II light-triggered robust carbon radical generation for combined photothermal and thermodynamic therapy of hypoxic tumors. *Adv Funct Mater* 2021;**31**:2101709.
39. Nel A, Xia T, Mädler L, Li N. Toxic potential of materials at the nanolevel. *Science* 2006;**311**:622.
40. Zhao Y, Gu X, Ma H, He X, Liu M, Ding Y. Association of glutathione level and cytotoxicity of gold nanoparticles in lung cancer cells. *J Phys Chem C* 2011;**115**:12797−802.
41. Lu Y, Yang Y, Gu Z, Zhang J, Song H, Xiang G, et al. Glutathione-depletion mesoporous organosilica nanoparticles as a self-adjuvant and co-delivery platform for enhanced cancer immunotherapy. *Biomaterials* 2018;**175**:82−92.
42. Ploemen JHTM, van Ommen B, van Bladeren PJ. Inhibition of rat and human glutathione *S*-transferase isoenzymes by ethacrynic acid and its glutathione conjugate. *Biochem Pharmacol* 1990;**40**:1631−5.
43. Shi X, Garcia GE, Neill RJ, Gordon RK. TCEP treatment reduces proteolytic activity of BoNT/B in human neuronal SHSY-5Y cells. *J Cell Biochem* 2009;**107**:1021−30.
44. Ling X, Tu J, Wang J, Shajii A, Kong N, Feng C, et al. Glutathione-responsive prodrug nanoparticles for effective drug delivery and cancer therapy. *ACS Nano* 2019;**13**:357−70.
45. Yang D, Chen M, Sun Y, Jin Y, Lu C, Pan X, et al. Microneedle-mediated transdermal drug delivery for treating diverse skin diseases. *Acta Biomater* 2021;**121**:119−33.
46. Chen M, Quan G, Wen T, Yang P, Qin W, Mai H, et al. Cold to hot: binary cooperative microneedle array-amplified photoimmunotherapy for eliciting antitumor immunity and the abscopal effect. *ACS Appl Mater Interfaces* 2020;**12**:32259−69.
47. Yang P, Lu C, Qin W, Chen M, Quan G, Liu H, et al. Construction of a core-shell microneedle system to achieve targeted co-delivery of checkpoint inhibitors for melanoma immunotherapy. *Acta Biomater* 2020;**104**:147−57.
48. Zhu J, Dong L, Du H, Mao J, Xie Y, Wang H, et al. 5-Aminolevulinic acid-loaded hyaluronic acid dissolving microneedles for effective photodynamic therapy of superficial tumors with enhanced long-term stability. *Adv Healthc Mater* 2019;**8**:1900896.
49. Pei P, Yang F, Liu J, Hu H, Du X, Hanagata N, et al. Composite-dissolving microneedle patches for chemotherapy and photothermal therapy in superficial tumor treatment. *Biomater Sci* 2018;**6**:1414−23.
50. Lan X, She J, Lin DA, Xu Y, Li X, Yang WF, et al. Microneedle-mediated delivery of lipid-coated cisplatin nanoparticles for efficient and safe cancer therapy. *ACS Appl Mater Interfaces* 2018;**10**:33060−9.
51. Hao Y, Chen YW, He XL, Yang F, Han RX, Yang CL, et al. Near-infrared responsive 5-fluorouracil and indocyanine green loaded MPEG-PCL nanoparticle integrated with dissolvable microneedle for skin cancer therapy. *Bioact Mater* 2020;**5**:542−52.
52. Lin S, Quan G, Hou A, Yang P, Peng T, Gu Y, et al. Strategy for hypertrophic scar therapy: improved delivery of triamcinolone acetonide using mechanically robust tip-concentrated dissolving microneedle array. *J Control Release* 2019;**306**:69−82.
53. Gong P, Wang Y, Zhang P, Yang Z, Deng W, Sun Z, et al. Immunocyte membrane-coated nanoparticles for cancer immunotherapy. *Cancers* 2021;**13**:77.
54. Akerman ME, Chan WCW, Laakkonen P, Bhatia SN, Ruoslahti E. Nanocrystal targeting *in vivo*. *Proc Natl Acad Sci U S A* 2002;**99**:12617−21.
55. Ghosh S. Cisplatin: the first metal based anticancer drug. *Bioorg Chem* 2019;**88**:102925.